Supporting Information

Dong et al. 10.1073/pnas.1708010115

Modeling the Stellar Wind of TRAPPIST-1

In this section, we describe the methodology involved in modeling the stellar wind of TRAPPIST-1 in more detail.

Description of the Alfvén Wave Solar Model. In this study, the TRAPPIST-1 stellar wind is simulated by means of the AWSoM (1), a data-driven global MHD model that was initially developed for simulating the solar atmosphere and solar wind. The inner boundary condition of the magnetic field can be specified by different magnetic maps from available observations. The initial conditions for the stellar wind plasma are determined through the Parker solution, while the initial magnetic field is based on the potential field source surface (PFSS) model with the finite-difference iterative potential solver (FDIPS) described in ref. 2.

Alfvén waves are driven at the inner boundary with a Poynting flux that scales with the surface magnetic field. The stellar wind is heated by Alfvén wave dissipation and accelerated by thermal and Alfvén wave pressure. Electron heat conduction (that includes both collisional and collisionless contributions) and radiative cooling are also included in the model. In the AWSoM, the electron and proton temperatures are treated separately, while the electrons and protons are assumed to have the same bulk velocity. However, heat conduction is applied only to the electrons, owing to their much higher thermal velocity. The system of governing equations is solved numerically using the BATS-R-US code within the Space Weather Modeling Framework (3).

By using a physically consistent treatment of wave reflection, dissipation, and heat partitioning between the electrons and protons, the AWSoM has successfully reproduced solar coronal conditions to a high degree of precision.

Application of the AWSoM to TRAPPIST-1. To adapt the AWSoM for TRAPPIST-1, we modify the rotational mass, radius, and period of the star in accordance with the latest observational data (4). Hence, we specify $M_\star = 0.08 M_\odot$, $R_\star = 0.11 R_\odot$, and $P_\star = 3.3$ d.

Due to the lack of direct surface magnetic-field observations of TRAPPIST-1, we use a solar magnetogram under the solar minimum condition (Global Oscillation Network Group magnetogram of Carrington Rotation 2077; ref. 5) and scale the mean and radial magnetic-field strength based on the magnetic-field observations of similar late M dwarfs (6). Based on the fact that the X-ray luminosity of TRAPPIST-1 is similar to that of the quiet Sun (7), we modify the Poynting flux parameter of the model such that the same amount of Poynting flux is generated as in the solar case. The simulation domain is extended to 250 $R_\star$ to ensure that the orbits of all seven planets in the TRAPPIST-1 system are duly encompassed.

Deducing the Magnetic Fields of the TRAPPIST-1 Planets

Since the past 40 y, it has been well known that radio emission from exoplanets can be used to detect them and thereby determine their magnetic fields (8). The basic idea behind detecting the planetary magnetic field (B_p) is that the cyclotron maser instability drives the emission of radio waves at a frequency approximately equal to the gyrofrequency (9). The maximum emission frequency ω is given by

$$\omega \approx \omega_c = \frac{eB}{m_e c}, \qquad \text{[S1]}$$

where m_e and e are the electron mass and charge, respectively. Hence, we propose that the radio auroral emission from the TRAPPIST-1 planets may be detectable by ground-based observatories when the frequency is above $\sim$10 MHz; the Earth's ionosphere reflects radio waves below this value, thereby requiring space- or lunar-based telescopes (10). As an illustrative example, let us suppose that $B_p \approx 0.1$ G for the TRAPPIST-1 planets, which leads us to $f = \omega/2\pi \approx 0.3$ MHz. This fiducial value is motivated by planetary dynamo scaling laws (11), as well as the lower limit of the hypothesized magnetic field for Proxima b (12).

Next, it is necessary to obtain a heuristic estimate of the radio flux density Φ at Earth to know whether the emission would be detectable. It can be estimated via

$$\Phi = \frac{P_{\rm radio}}{4\pi \Delta f D^2}, \qquad \text{[S2]}$$

where bandwidth $\Delta f \approx f/2$, D is the distance to Earth, and $P_{\rm radio}$ represents the planetary radio power (13). Thus, a knowledge of $P_{\rm radio}$ and ω would suffice to determine Φ. Although there exist several ways of computing $P_{\rm radio}$ (10), it has been noted that the planetary radio power is dominated by the dissipation of the magnetic power carried by the stellar wind (14),

$$P_{\rm radio} \sim 2 \times 10^{-3} \left(\frac{\pi B_{sw}^2 r_m^2 V_{sw}}{4\pi} \right), \qquad \text{[S3]}$$

where B_{sw} is the interplanetary magnetic field (IMF) and V_{sw} is the stellar wind velocity, and both of them are listed in Table S2. Here, r_m denotes the planetary magnetospheric radius and is given by

$$r_m = R_p \left(\frac{B_p^2}{8\pi P_{sw}} \right)^{1/6}, \qquad \text{[S4]}$$

where $P_{sw} \approx \rho_{sw} v_{sw}^2$ is the dynamical pressure and ρ_{sw} is the stellar wind density provided in Table S2. Hence, it is possible to combine Eqs. **S2**–**S4** to arrive at an estimate of Φ. We find that the radio flux density, for the above choice of values, is $\mathcal{O}\left(10^{-4}\right)$ Jy. However, we note that Φ can be boosted by a factor of $\sim 10^2 - 10^3$ during a large CME event, which would imply that it can attain a value of $\sim 10-100$ mJy. This follows from the fact that the stellar wind parameters are enhanced during a CME event, and the corresponding radio power is also increased accordingly (15). We note that a similar approach has also been used in the context of Proxima b, where it was shown that the radio flux density attained a peak value of $\sim 1-10$ Jy during a large Carrington-type CME event.

Thus, to summarize, future space-based (or lunar) low-frequency observations may be able to constrain the planetary magnetic fields of the TRAPPIST-1 planets by measuring the radio flux density and extrapolating backward to determine the value of B_p.

Atmospheric Ion Escape Rates for the TRAPPIST-1 Planets

In this section, we briefly describe the workings of the code and provide additional results pertaining to the atmospheric ion escape rates.

Physical Model and Computational Methodology. The 3D BATS-R-US MS-MHD model was initially developed in the context of our Solar System, i.e., for studying Mars (16) and Venus (17). We rely upon the code developed for Venus, and the neutral atmospheric profiles are based on the solar maximum conditions. The MS-MHD comprises a separate continuity equation for each ion species in conjunction with one momentum equation and one energy equation for the four ion fluids H^+, O^+, O_2^+, and CO_2^+

(16, 17). Unlike most global (Earth) magnetosphere models that commence from two to three Earth radii, the Mars/Venus MS-MHD model contains a self-consistent ionosphere, and thus the lower boundary extends down to an altitude of 100 km above the planetary surface. The MS-MHD model, which serves as the basis of our paper, accounts for a diverse array of chemical processes, such as charge exchange, photoionization, and electron recombination.

The various chemical reactions and their corresponding rate coefficients have been delineated in Table S1, and the reader may also consult ref. 18 for further details. The densities of O^+, O_2^+, and CO_2^+ at the lower boundary satisfy the photochemical equilibrium condition as described in ref. 18. The model also assumes that the plasma temperature (sum of ion and electron temperatures) is approximately double that of the neutral temperature at the lower boundary because of the high collision frequency.

The grid is also taken to be nonuniform and spherical in nature to accurately capture the multiscale physics operating in different regions. Hence, the radial resolution ranges from around half the scale height at the lower boundary to several thousands of kilometers at the outer boundary. The horizontal resolution is chosen to be 3.0° (in both longitude and latitude), while the simulation domain ranges between $-45\,R_x \le X \le 15\,R_x$ and $-30\,R_x \le Y, Z \le 30\,R_x$, where R_x denotes the radius of planet X. The code is run in the planet–star-orbital (PSO) coordinate system, where the x axis is directed from the planet toward TRAPPIST-1, the z axis is perpendicular to the planet's orbital plane, and the y axis completes the right-hand system.

The multispecies MHD equations are summarized as

$$\frac{\partial \rho_s}{\partial t} + \nabla \cdot (\rho_s \mathbf{u}) = \mathcal{S}_s - \mathcal{L}_s \qquad \textbf{[S5]}$$

$$\frac{\partial (\rho \mathbf{u})}{\partial t} + \nabla \cdot \left(\rho \mathbf{u}\mathbf{u} + p\mathbf{I} + \frac{B^2}{2\mu_0}\mathbf{I} - \frac{1}{\mu_0}\mathbf{B}\mathbf{B} \right) = \rho \mathbf{G} - \sum_{s=ions} \rho_s \sum_{n=neutrals} \nu_{sn}\mathbf{u} - \sum_{s=ions} \mathcal{L}_s \mathbf{u} \qquad \textbf{[S6]}$$

$$\frac{\partial}{\partial t}\left(\frac{\rho u^2}{2} + \frac{p}{\gamma - 1} + \frac{B^2}{2\mu_0} \right) + \nabla \cdot \left[\left(\frac{\rho u^2}{2} + \frac{\gamma p}{\gamma - 1} + \frac{B^2}{\mu_0} \right) \mathbf{u} - \frac{(\mathbf{B} \cdot \mathbf{u})\mathbf{B}}{\mu_0} + \mathbf{B} \times \frac{\nabla \times \mathbf{B}}{\mu_0^2 \sigma_0} \right] \qquad \textbf{[S7]}$$

$$= \sum_{s=ions} \sum_{n=neutrals} \frac{\rho_s \nu_{sn}}{m_s + m_n} \left[3k\,(T_n - T_s) - m_s u^2 \right] + \rho \mathbf{u} \cdot \mathbf{G} + \frac{k}{\gamma - 1} \sum_{s=ions} \frac{(\mathcal{S}_s T_n - \mathcal{L}_s T_s)}{m_s} - \frac{1}{2} \sum_{s=ions} \mathcal{L}_s u^2 + \frac{k}{\gamma - 1} \frac{\mathcal{S}_e T_{n0} - \mathcal{L}_e T_e}{m_e}$$

$$\frac{\partial \mathbf{B}}{\partial t} + \nabla \cdot (\mathbf{u}\mathbf{B} - \mathbf{B}\mathbf{u}) = -\nabla \times \left(\frac{1}{\mu_0 \sigma_0} \nabla \times \mathbf{B} \right), \qquad \textbf{[S8]}$$

where Eqs. **S5**, **S6**, and **S7** represent the conservation of mass (of each species), momentum, and energy, respectively, while Eq. **S8** is the magnetic induction equation. The total mass density is $\rho = \sum_{s=ions} \rho_s$ and ν_{sn} is the elastic ion-neutral collision frequency (16, 17). The ratio of the specific heats γ is taken to be 5/3. The subscripts s, n, and e indicate ion species s, neutral species n, and electron e. The other symbols have their usual definitions (16, 17). To account for photoionization, we calculate the optical depth of the neutral atmosphere by applying the Chapman functions based on the numerical evaluation given by ref. 20. The photoelectron gains an excess energy through the photoionization process, as indicated by the presence of T_{n0} in Eq. **S7**. Therefore, we include the stellar heating via photoionization as the conventional hydrodynamic models (e.g., ref. 21). In the above set of equations, note that the source ($\mathcal{S}$) and loss ($\mathcal{L}$) terms of species s associated with photoionization ($\nu_{ph,s'}$), charge exchange ($k_{is'}$), and recombination ($\alpha_{R,s}$) are shown as follows:

$$\mathcal{S}_s = m_s n_{s'} \left(\nu_{ph,s'} + \sum_{i=ions} k_{is'} n_i \right) \qquad \textbf{[S9]}$$

$$\mathcal{L}_s = m_s n_s \left(\alpha_{R,s} n_e + \sum_{n'=neutrals} k_{sn'} n_{n'} \right) \qquad \textbf{[S10]}$$

$$\mathcal{S}_e = m_e \sum_{s'=neutrals} \nu_{ph,s'} n_{s'} \qquad \textbf{[S11]}$$

$$\mathcal{L}_e = m_e n_e \sum_{s=ions} \alpha_{R,s} n_s. \qquad \textbf{[S12]}$$

In Eq. **S8**, σ_0 is the electrical conductivity. In the model, the electrical conductivity in the planetary ionosphere is calculated using

$$\sigma_0 = \frac{n_e e^2}{m_e(\nu_{ei} + \nu_{en})}, \qquad \textbf{[S13]}$$

where m_e is the electron mass, and ν_{ei} and ν_{en} are the electron–ion and electron–neutral collision frequencies, respectively. The collision frequencies ν_{ei} and ν_{en} are given by ref. 17:

$$\nu_{ei} = 54.5 \frac{n_i}{T_e^{3/2}}, \qquad \textbf{[S14]}$$

$$\nu_{en} = 3.68 \times 10^{-8} \left(1 + 4.1 \times 10^{-11} |4{,}500 - T_e|^{2.93}\right) [CO_2] + 8.9 \times 10^{-11} (1 + 5.7 \times 10^{-4}\, T_e)\, T_e^{1/2} [O]. \qquad \textbf{[S15]}$$

The above set of equations is solved using an upwind finite-volume scheme based on an approximate Riemann solver, to ensure the appropriate conservation of plasma variables. To determine the steady-state solution, the simulation starts with a two-stage local-time stepping scheme that enables different grid cells to select different advance time steps, thus accelerating convergence to the steady state to save computational resources. Because of the stiffness of the source terms, a point implicit scheme is used for handling them.

Auxiliary Results. In the main text, the atmospheric ion escape rates are provided for two cases: (*i*) maximum dynamic and total pressure and (*ii*) minimum total pressure, but maximum magnetic pressure. The corresponding stellar wind parameters for these two cases are delineated in Table S2.

In Table S2, note that N_{sw}, T_{sw}, and V_{sw} denote the number density, temperature, and velocity of the stellar wind, respectively, at the locations of the seven planets, whereas IMF denotes the interplanetary magnetic field. The case with minimum total pressure corresponds to the fast solar wind, which features a higher velocity albeit with a lower density, whereas the converse is true for the maximum total pressure that can be associated with the slow solar wind.

In Fig. S1, the ionospheric profiles for TRAPPIST-1g are provided for the cases with minimum and maximum total pressure. An inspection of Table S2 reveals that the cases with minimum and maximum total pressure have very different stellar wind parameters, for, e.g., density, velocity, and IMF. Despite the considerable variability in the stellar wind parameters, it is evident that the ionospheric profiles remain mostly unaffected. This would appear to indicate that the lower regions are effectively immune to the effects of the stellar wind, which lends some credibility to the fact that surface biological processes (if present) may not be significantly affected.

1. van der Holst B, et al. (2014) Alfvéen Wave Solar Model (AWSoM): Coronal Heat. *Astrophys J* 782:81.
2. Tćoth G, van der Holst B, Huang Z (2011) Obtaining potential field solutions with spherical harmonics and finite differences. *Astrophys J* 732:102.
3. Tćoth G, et al. (2012) Adaptive numerical algorithms in space weather modeling. *J Comp Phys* 231:870–903.
4. Luger R, et al. (2017) A seven-planet resonant chain in TRAPPIST-1. *Nat Astron* 1:0129.
5. Jin M, et al. (2012) A global two-temperature corona and inner heliosphere model: A comprehensive validation study. *Astrophys. J* 745:6.
6. Morin J, et al. (2010) Large-scale magnetic topologies of late M dwarfs. *Mon Not R Astron Soc* 407:2269–2286.
7. Bourrier V, et al. (2017) Reconnaissance of the TRAPPIST-1 exoplanet system in the Lyman-α line. *Astron Astrophys* 599:L3.
8. Yantis WF, Sullivan WT, III, Erickson WC (1977) A search for extra-solar Jovian planets by radio techniques. *Bull Am Astron Soc* 9:453.
9. Zarka P (1998) Auroral radio emissions at the outer planets: Observations and theories. *J Geophys Res* 103:20159–20194.
10. Grießmeier J-M (2015) Detection methods and relevance of exoplanetary magnetic fields. *Characterizing Stellar and Exoplanetary Environments*, Astrophysics and Space Science Library, eds Lammer H, Khodachenko M (Springer, Heidelberg), Vol 411, pp 213–237.
11. Christensen UR (2010) Dynamo scaling laws and applications to the planets. *Space Sci Rev* 152:565–590.
12. Burkhart B, Loeb A (2017) The detectability of radio auroral emission from Proxima b. *Astrophys J Lett* 849:L10.
13. Zarka P (2007). Plasma interactions of exoplanets with their parent star and associated radio emissions. *Planet Space Sci* 55:598–617.
14. Vidotto AA, Donati J-F (2017) Predicting radio emission from the newborn hot Jupiter V830 Tauri b and its host star. *Astron Astrophys* 602:A39.
15. Grießmeier J-M, Zarka P, Spreeuw H (2007) Predicting low-frequency radio fluxes of known extrasolar planets. *Astron Astrophys* 475:359–368.
16. Ma Y, Nagy AF, Sokolov IV, Hansen KC(2004) Three-dimensional, multispecies, high spatial resolution MHD studies of the solar wind interaction with Mars. *J Geophys Res A* 109:A07211.
17. Ma YJ, et al. (2013) A global multispecies single-fluid MHD study of the plasma interaction around Venus. *J Geophys Res A* 118:321–330.
18. Dong C, Lingam M, Ma Y, Cohen O (2017) Is Proxima Centauri b habitable? A study of atmospheric loss. *Astrophys J Lett* 837:L26.
19. Bolmont E, et al. (2017) Water loss from terrestrial planets orbiting ultracool dwarfs: Implications for the planets of TRAPPIST-1. *Mon Not R Astron Soc* 464: 3728–3741.
20. Smith FL, Smith C (1972) Numerical evaluation of Chapman's grazing incidence integral ch (X, χ). *J Geophys Res* 77:3592–3597.
21. Tripathi A, Kratter KM, Murray-Clay RA, Krumholz MR (2015) Simulated photoevaporative mass loss from hot Jupiters in 3D. *Astrophys J* 808:173.

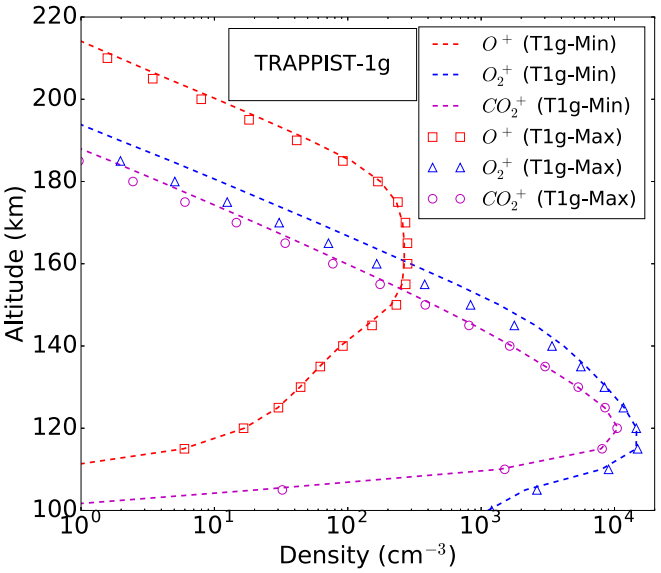

Fig. S1. The ionospheric profiles along the substellar line for TRAPPIST-1g for the cases of (*i*) maximum and (*ii*) minimum total pressure over its orbit.

Table S1. Chemical reactions and associated rates adapted from ref. 18

Chemical reaction	Rate coefficient
Primary photolysis in s^{-1}	
$CO_2 + h\nu \rightarrow CO_2^+ + e^-$	See table legend
$O + h\nu \rightarrow O^+ + e^-$	See table legend
Ion-neutral chemistry in $cm^3\ s^{-1}$	
$CO_2^+ + O \rightarrow O_2^+ + CO$	1.64×10^{-10}
$CO_2^+ + O \rightarrow O^+ + CO_2$	9.60×10^{-11}
$O^+ + CO_2 \rightarrow O_2^+ + CO$	$1.1 \times 10^{-9}\ (800/T_i)^{0.39}$
$H^+ + O \rightarrow O^+ + H$	5.08×10^{-10}
Electron recombination chemistry in $cm^3 \cdot s^{-1}$	
$O_2^+ + e^- \rightarrow O + O$	$7.38 \times 10^{-8}\ (1{,}200/T_e)^{0.56}$
$CO_2^+ + e^- \rightarrow CO + O$	$3.10 \times 10^{-7}\ (300/T_e)^{0.5}$

The photoionization frequencies are rescaled to account for the EUV fluxes received at each of the TRAPPIST-1 planets based on the estimates provided in refs. 7 and 19.

Table S2. Stellar wind parameters for the TRAPPIST-1 planets

Total pressure	N_{sw}, cm^{-3}	T_{sw}, K	V_{sw}, km/s	IMF, nT
Maximum total pressure				
Trappist-1b	6.59×10^4	2.01×10^6	(−470, 80, −1)	(381, 81, −147)
Trappist-1c	2.99×10^4	1.68×10^6	(−527, 68, 0)	(210, 42, −111)
Trappist-1d	1.20×10^4	1.59×10^6	(−566, 56, 6)	(−129, 15, −50)
Trappist-1e	5.79×10^3	1.26×10^6	(−604, 50, 3)	(−149, 13, −42)
Trappist-1f	2.99×10^3	1.02×10^6	(−624, 44, 3)	(−98, 7, −34)
Trappist-1g	1.95×10^3	8.92×10^5	(−637, 40, 2)	(−69, 6, −28)
Trappist-1h	9.52×10^2	7.17×10^5	(−657, 37, 2)	(−44, 2, −25)
Minimum total pressure				
Trappist-1b	4.28×10^3	2.40×10^6	(−803, 80, 10)	(−2206, 96, −64)
Trappist-1c	2.09×10^3	2.35×10^6	(−871, 68, −3)	(−1192, 63, −64)
Trappist-1d	1.06×10^3	2.00×10^6	(−923, 56, −5)	(−641, 41, −59)
Trappist-1e	5.68×10^2	1.72×10^6	(−972, 50, 3)	(−379, 32, −38)
Trappist-1f	2.93×10^2	1.44×10^6	(−1017, 44, 19)	(−218, 23, −25)
Trappist-1g	2.05×10^2	1.30×10^6	(−1032, 40, 2)	(−159, 20, −19)
Trappist-1h	1.09×10^2	1.07×10^6	(−1049, 37, −16)	(−89, 14, −11)